Aust. J. Phys., 1991, **44**, 441–58

Effect of Source Morphology on Thermal Radio Continuum Spectra

Mark Calabretta

School of Physics, University of Sydney,
Sydney, N.S.W. 2006, Australia.
Present address: Australia Telescope National Facility, CSIRO,
P.O. Box 76, Epping, N.S.W. 2121, Australia.

Abstract

The thermal radio continuum spectra derived from a selection of nebular models are compared. One class of models arises from three-dimensional distributions of emissivity, while the remainder are specified in a more abstract way. It is shown that the most important distinguishing feature between the models is the proportion of the nebular solid angle occupied by very faint emission. This finding is developed into a measure of nebular clumping. Practical aspects of the modelling are examined by applying a selection of the model spectra to the flux densities observed for the planetary nebula IC 418.

1. Introduction

It has long been recognised that the shape of the radio continuum spectrum of a thermal source, such as an HII region or planetary nebula, is governed by the distribution of emitting material as seen by the observer. In fitting model spectra to the observed radio flux densities, the nebular morphology must therefore be known or some assumptions made concerning it. However, the detailed morphological information required is often not available, and past workers have resorted to using simple models, such as that of a uniform filled sphere, or more elaborate ones consisting of concentric shells of varying emissivity.

The geometric parameters which must be specified in constructing these models must be inferred from optical images of the particular nebula and hence are not known with any certainty. Indeed, it could happen that the model adopted is entirely inappropriate to the actual morphology. The question thus arises as to the importance of the choice of model.

Several models of nebular morphology are examined in this paper, and the resulting spectra are presented graphically. A selection of models is then applied to the actual radio continuum flux densities observed for the planetary nebula IC 418 and the results compared.

2. Theory

The radio flux density S_ν, at frequency ν, of an isothermal nebula with electron temperature T_e is given by

$$S_\nu = \frac{2kT_e\nu^2}{c^2}\Omega_s\eta_\nu, \qquad (1)$$

0004-9506/91/040441$05.00

where k is Boltzmann's constant, c is the velocity of light, and

$$\eta_\nu = \frac{1}{\Omega_s} \int \{1 - \exp[-\tau_\nu(\theta,\phi)]\}\, d\theta\, d\phi . \tag{2}$$

The integral is evaluated over the solid angle of the source Ω_s, and $\tau_\nu(\theta,\phi)$ describes the two-dimensional distribution of optical depth at frequency ν. Coordinates (θ,ϕ) are a convenient Cartesian system.

Since $\tau_\nu(\theta,\phi) \geq 0$, we must have $0 \leq \eta_\nu \leq 1$. Referring to equation (1), we see that η_ν is a measure of the departure of the nebula from a black-body radiator. Note that if $\tau_\nu(\theta,\phi) \gg 1$ over Ω_s then $\eta_\nu \approx 1$, whereas if $\tau_\nu(\theta,\phi) \ll 1$ then $\eta_\nu \approx \langle\tau_\nu\rangle$, where the angle brackets denote averaging over Ω_s,

$$\langle\tau_\nu\rangle = \frac{1}{\Omega_s} \int \tau_\nu(\theta,\phi)\, d\theta\, d\phi . \tag{3}$$

The critical frequency ν_c is defined at the intersection of the two regimes so that $\langle\tau_\nu\rangle = 1$ at $\nu = \nu_c$.

To apply equations (1) and (2) we need to know how $\tau_\nu(\theta,\phi)$ varies with ν, and this was given by Oster (1961) as

$$\tau_\nu(\theta,\phi) = \frac{8}{3(2\pi)^{1/2}} \frac{Z^2 e^6 \nu^{-2}}{c(mkT_e)^{3/2}} \ln\left[\frac{2(2kT_e)^{3/2}}{5\pi e^{-\gamma} m^{1/2} e^2 Z\nu}\right] E(\theta,\phi), \tag{4}$$

where Z (=1) is the atomic number, e and m are the electron charge and mass, γ (=0·577) is Euler's constant and $E(\theta,\phi)$ is the emission measure, defined as an integral of the product of the electron and ion densities along the line of sight through the nebula,

$$E(\theta,\phi) = \int N_e(\theta,\phi,z) N_i(\theta,\phi,z)\, dz . \tag{5}$$

Equation (4) is difficult to use since T_e and ν appear in the argument of the logarithm. A close approximation to it was given by Altenhoff *et al.* (1960),

$$\tau_\nu(\theta,\phi) = 0{\cdot}082\, Z^{1{\cdot}9} T_e^{-1{\cdot}35} \nu^{-2{\cdot}10} E(\theta,\phi) \tag{6}$$

for T_e in K, ν in GHz, and E in pc cm^{-6}. As shown in Table 6 of Mezger and Henderson (1967), the error in equation (6) is mostly <2% in the range 300 MHz to 10 GHz for temperatures between 6000 and 14,000 K.

Since the frequency dependence of $\tau_\nu(\theta,\phi)$ is independent of the spatial distribution we may write

$$\tau_\nu(\theta,\phi) = \langle\tau_\nu\rangle \tau(\theta,\phi), \tag{7}$$

so that $\langle\tau(\theta,\phi)\rangle = 1$. Considering equations (1) and (2), we see that $\tau_\nu(\theta,\phi)$ enters into the determination of S_ν only through an integral over the surface of the nebula. This means that it is unnecessary to have the detailed two-dimensional information implicit in $\tau_\nu(\theta,\phi)$. For instance, if $\tau(\theta,\phi)$ is represented by a pixel map, the pixels within Ω_s may be rearranged spatially

without affecting the results. Alternatively, if the pixels were lined up in decreasing order of pixel height, a function $\tau(\Omega)$ of a solid angle variable Ω would be obtained, and this would contain all of the essential morphological information of $\tau(\theta,\phi)$. It is then natural to work in terms of

$$\omega = \frac{\Omega}{\Omega_s}. \tag{8}$$

Specifying $\tau(\omega)$ thus determines an infinite equivalence class of nebular morphologies which may look very different, but which are similar in terms of their radio continuum spectra. Equation (2) may be rewritten as

$$\eta_\nu = \int_0^1 \{1 - \exp[-\tau_\nu(\omega)]\}\, d\omega. \tag{9}$$

Likewise, combining equations (6) and (7) we have

$$\tau_\nu(\omega) = \langle \tau_\nu \rangle \tau(\omega) = \left(\frac{\nu}{\nu_c}\right)^{-2\cdot 1} \tau(\omega). \tag{10}$$

To compare the radio spectra of two models defined by $\tau_1(\omega)$ and $\tau_2(\omega)$, we might fix T_e, Ω_s, and ν_c at some arbitrary values and compute S_ν as a function of ν for each. The two spectra should differ from one another only where they turn over from being optically thick to optically thin. Alternatively, to avoid having to specify T_e and Ω_s, it is useful to normalise S_ν by dividing by s_ν, where

$$s_\nu = \frac{2kT_e\nu^2}{c^2}\Omega_s\langle\tau_\nu\rangle; \tag{11}$$

s_ν is effectively the extrapolation of the optically thin part of the radio spectrum to all frequencies. The modified spectrum ϑ_ν, which is asymptotic to unity at high frequencies, is given by

$$\vartheta_\nu = \frac{S_\nu}{s_\nu} = \frac{\eta_\nu}{\langle\tau_\nu\rangle}; \tag{12}$$

ϑ_ν might be thought of as a '*transparency*', since it it unity in the optically thin regime and decreases towards zero with increasing optical depth.

If the value of ν_c is given, the spectrum of ϑ_ν versus ν corresponding to $\tau(\omega)$ can be constructed through equations (9), (10) and (12). In turn, the observed radio flux densities can be fitted to this spectrum of ϑ_ν by specifying s_0, the value of s_ν at some standard frequency ν_0. In practice, the best-fit values of ν_c and s_0 would be found via the least-squares or maximum likelihood methods of estimation. Note that approximate values of these two parameters could be measured directly from an adequately observed radio spectrum. The value of s_0 is determined by flux densities in the optically thin regime and these are often fairly accurate. On the other hand, the determination of ν_c relies also on observations at or below the turnover region of the spectrum, and these are usually fewer and less accurate. Once s_0 and ν_c are known and

Ω_s provided, T_e may be computed via equations (10) and (11). The emission measure may then be derived from equation (6).

The inverse of $\tau(\omega)$ may be written as $\omega(\tau)$, a function which gives the fraction of the source solid angle occupied by regions of the nebula with normalised optical depth exceeding τ. By following Salem and Seaton (1974), ϑ_ν can be expressed explicitly in terms of $\omega(\tau)$. Combining equations (9) and (12) and integrating by parts, noting that $\tau_\nu = 0$ at $\omega = 1$, and $\omega(\tau) = 0$ for $\tau \geq \tau_{max}$, we have a Laplace transform

$$\vartheta_\nu = \int_0^\infty \omega(\tau) \exp(-\tau\langle\tau_\nu\rangle)\, d\tau. \tag{13}$$

If ϑ_ν is known with sufficient accuracy, equation (13) can be inverted to obtain $\omega(\tau)$. Unfortunately, this is not practical for observed radio spectra, since $\omega(\tau)$ is extremely sensitive to inaccuracies in ϑ_ν.

3. Models

Two types of model are presented. Members of the first group are constructed simply by specifying the functional form of $\tau(\omega)$. The others are derived from three-dimensional, radially symmetric models of the radio source. Profiles of $\tau(\omega)$ and the corresponding spectra of ϑ_ν are presented in Figs 1 to 8. Each model is properly normalised so that $\langle\tau(\omega)\rangle = 1$, and $\tau(\omega)$ is set to zero outside the interval $0 \leq \omega \leq 1$. The model spectra of ϑ_ν versus ν are constructed using the assumption that $\nu_c = 1$ GHz. Their parametrisation by $\langle\tau_\nu\rangle$ and η_ν, constructed via equations (10) and (12), is also shown.

Some of the models to be discussed here do not have a natural boundary for the definition of Ω_s. This is an artefact of the mathematical formulation of the model since, in reality, Ω_s cannot exceed 4π sr. In practice, the source solid angle is constrained by the uncertainties of measurement since arbitrarily large, vanishingly faint haloes cannot be observed. Thus for models with no natural boundary a cutoff needs to be imposed.

(a) The Uniform Slab

This is the simplest possible model and is defined by $\tau(\omega) = 1$ for $0 \leq \omega \leq 1$, and $\tau(\omega) = 0$ otherwise. Nevertheless it is important, since its spectrum is an extreme case among all possible models. In fact, *the spectrum of a uniform slab has the sharpest possible turnover in the sense that, for any value of* $\langle\tau_\nu\rangle$, ϑ_ν *is higher for a slab than for any other distribution.*

To prove this, consider equation (13) and let $\omega_u(\tau)$ denote the uniform slab, and $\omega(\tau)$ the other distribution. Then we have

$$\begin{aligned}
\vartheta_\nu(\text{slab}) - \vartheta_\nu(\text{other}) &= \int_0^\infty (\omega_u - \omega) \exp(-\tau\langle\tau_\nu\rangle)\, d\tau \\
&= \int_0^1 (1-\omega) \exp(-\tau\langle\tau_\nu\rangle)\, d\tau - \int_1^\infty \omega \exp(-\tau\langle\tau_\nu\rangle)\, d\tau \\
&\geq \exp(-\langle\tau_\nu\rangle)\left[\int_0^1 (1-\omega)\, d\tau - \int_1^\infty \omega\, d\tau\right] \\
&= 0.
\end{aligned}$$

The uniform slab is included in Fig. 1 as a special case of the next set of models.

(b) Core–Halo Models

Core–halo models are defined so that the optical depth is constant within a core region and constant but at a lower level in the halo region. Two parameters are required; ω_c defines the relative size of the core and ρ the ratio of optical depths. Figs 1 and 2 show how the spectra change as these parameters are varied.

(c) Exponential Models

These models are defined by $\tau(\omega) = a \exp(-\omega/\omega_e)$, where ω_e is a parameter and a a normalising constant which depends on ω_e. The exponential form of $\tau(\omega)$ would arise if $\tau_\nu(\theta,\phi)$ had a Gaussian profile in two dimensions. In turn, this form of $\tau_\nu(\theta,\phi)$ could arise if the radial (r) dependence of electron density varied as $\exp(-r/r_0)$ in a spherically symmetric nebula in three dimensions. However, these are special cases, and wildly different morphologies could produce the exponential form of $\tau(\omega)$. Fig. 3 shows the profiles and spectra of a set of exponential models.

(d) Power-law Models

Models defined by $\tau(\omega) = \delta[(\omega-\omega_u)/(1-\omega_u)]^{-\gamma}$ are relevant to mass-loss stars although Pottasch (1984) has applied them to the planetary nebula NGC 2440. Panagia and Felli (1975), Wright and Barlow (1975) and Olnon (1975) used them to explain why objects like P Cygni, T Tauri, V1016 Cygni and MWC 349 have radio spectra with spectral index $\alpha \approx +0{\cdot}7$ over a large range of frequencies. They showed that this arises naturally if the electron density falls off slightly faster than the inverse square of the distance from the star.

The power-law models presented in Fig. 4 cutoff explicitly at $\omega = 1$, at which point $\tau = \delta$, where δ is a free parameter chosen to be very small. The power-law divergence at zero radius was handled by past workers by assuming a core region of uniform electron density. In effect, this core allows the computed spectrum to reach the normal optically thin regime at high frequencies, otherwise the spectrum would diverge. However, it is not necessary to make any assumptions about what happens in the core since it should be of negligible angular extent, so long as the electron density does not diverge. In the present treatment the core region is simply excluded through the introduction of ω_u. Its value is chosen to normalise $\tau(\omega)$.

(e) Uniform Shell Models

As yet nothing has been said about the three-dimensional structure of a nebula and how this affects the radio continuum spectrum. In the absence of information regarding the distribution of optical depth over the face of a nebula, the procedure often adopted is to assume a sphere of uniform emissivity. A refinement is to use a uniform shell based on an assumed or observed parameter ϕ, the ratio of shell thickness to exterior radius. The case $\phi = 1$ is a uniform sphere.

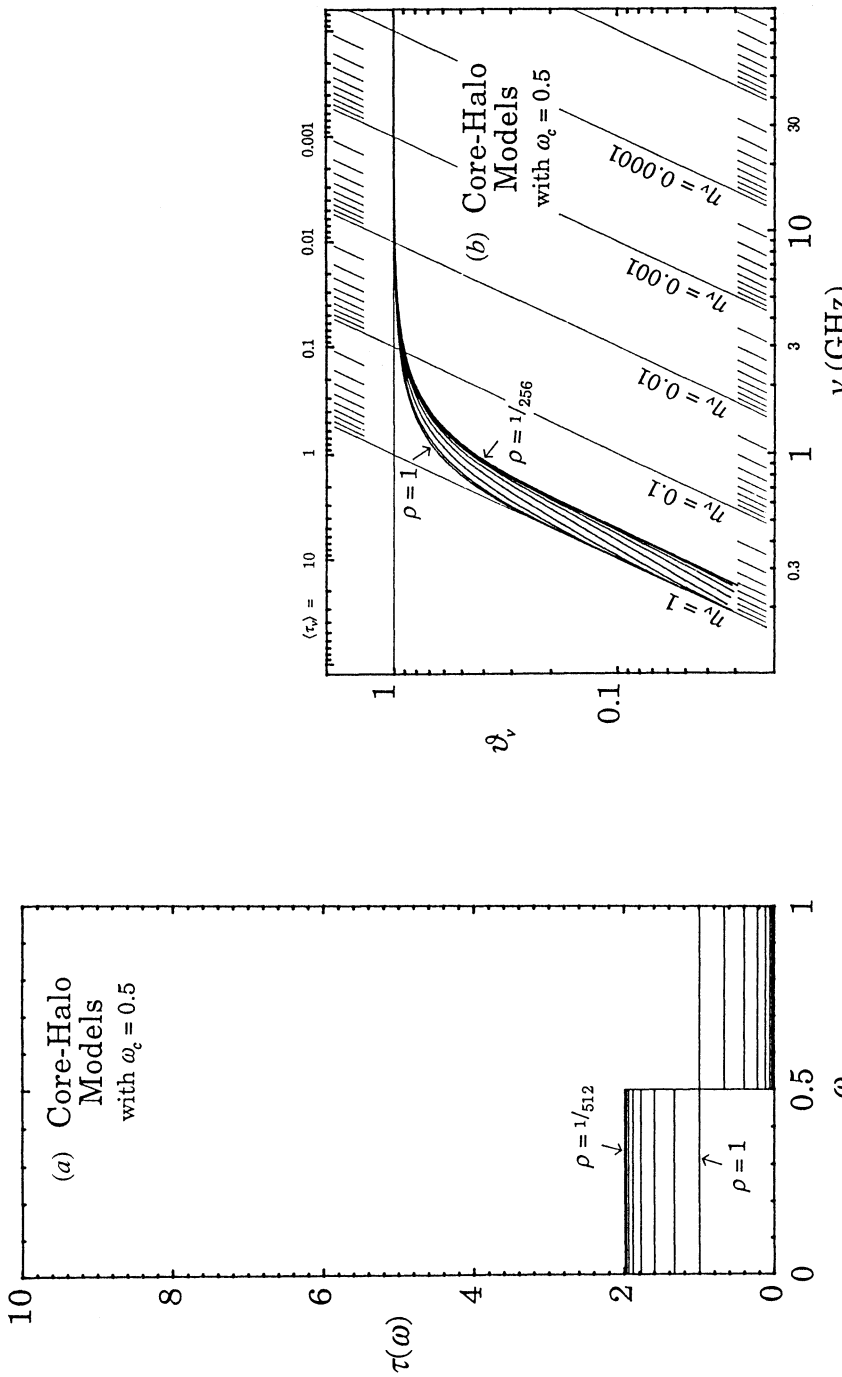

Fig. 1*a*. Profiles of $\tau(\omega)$ for core–halo models with $\omega_c = 1/2$ and $\rho = 1, 1/2, \ldots 1/512$. The case with $\rho = 1$ is a uniform slab.
Fig. 1*b*. The spectra of ϑ_ν derived from the core–halo models of Fig. 1*a*.

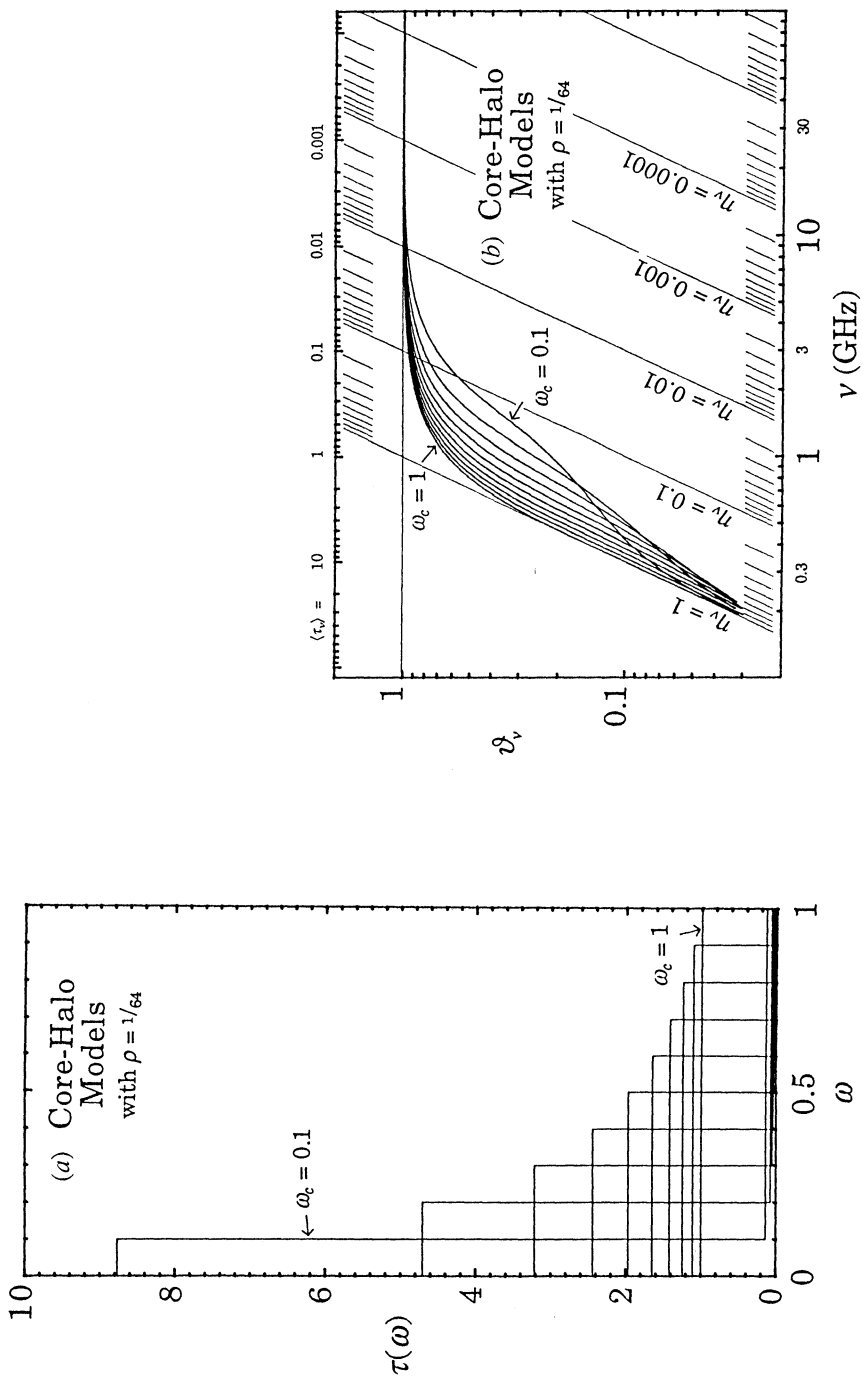

Fig. 2a. Profiles of $\tau(\omega)$ for core-halo models with $\omega_c = 0{\cdot}1$, $0{\cdot}2$,... $1{\cdot}0$ and $\rho = 1/64$. The case with $\omega_c = 1$ is a uniform slab.
Fig. 2b. The spectra of ϑ_ν derived from the core-halo models of Fig. 2*a*.

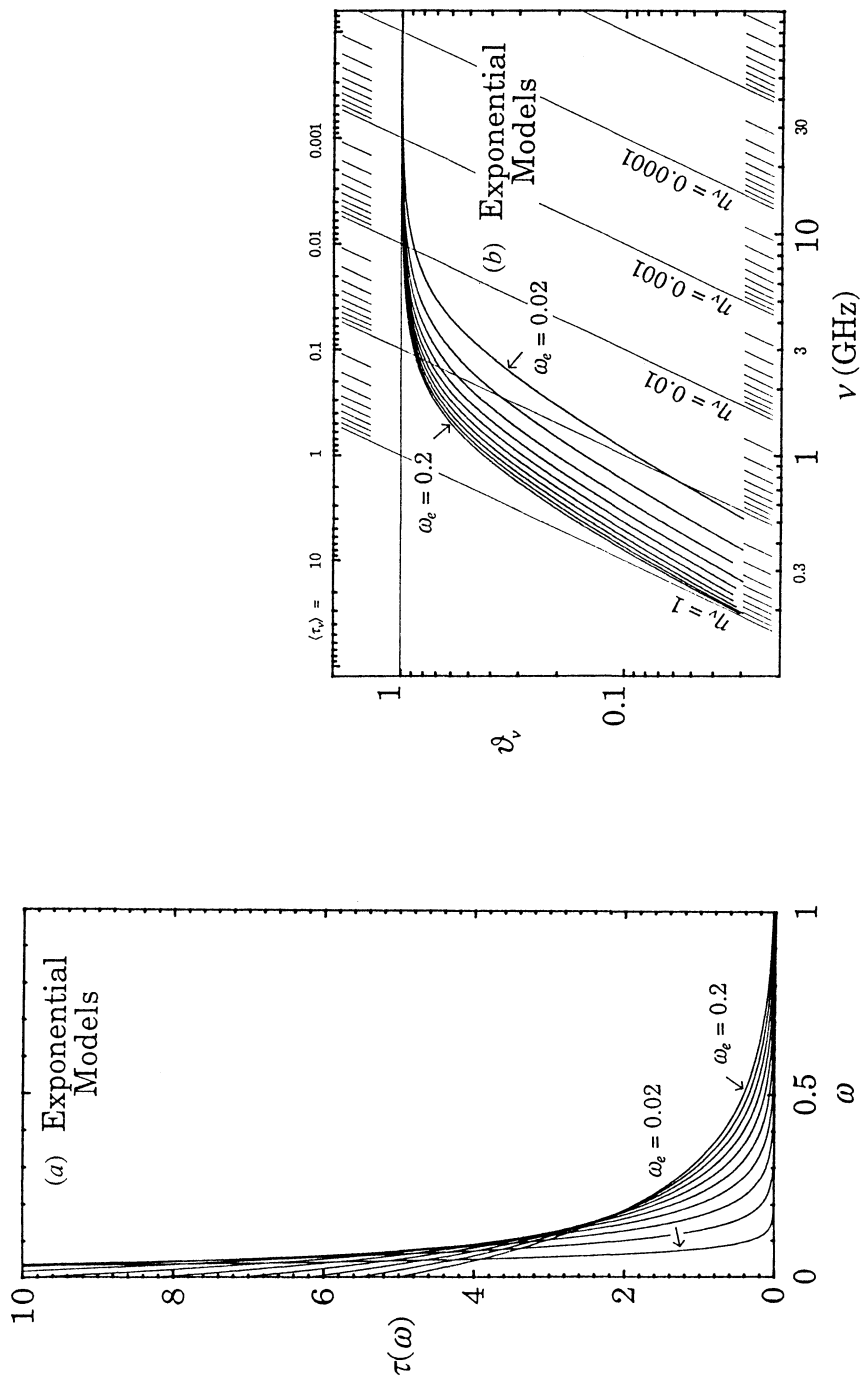

Fig. 3*a*. Profiles of $\tau(\omega)$ for exponential models with $\omega_e = 0{\cdot}02,\ 0{\cdot}04, \ldots\ 0{\cdot}20$.
Fig. 3*b*. The spectra of ϑ_ν derived from the exponential models of Fig. 3*a*.

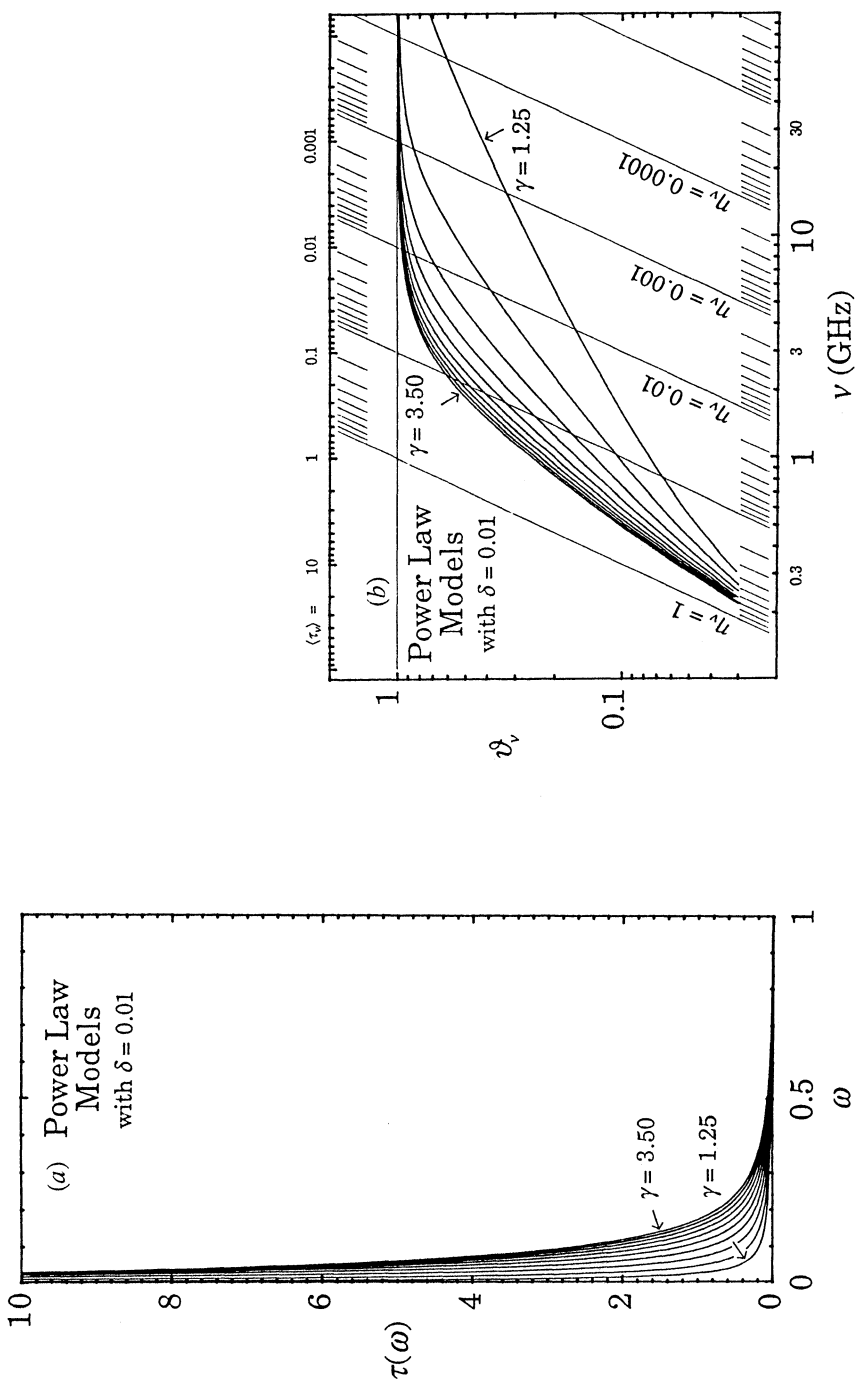

Fig. 4a. Profiles of $\tau(\omega)$ for power-law models with $\delta = 0{\cdot}01$, and $\gamma = 1{\cdot}25,\ 1{\cdot}50,\ldots\ 3{\cdot}50$.
Fig. 4b. The spectra of ϑ_ν derived from the power-law models of Fig. 4*a*.

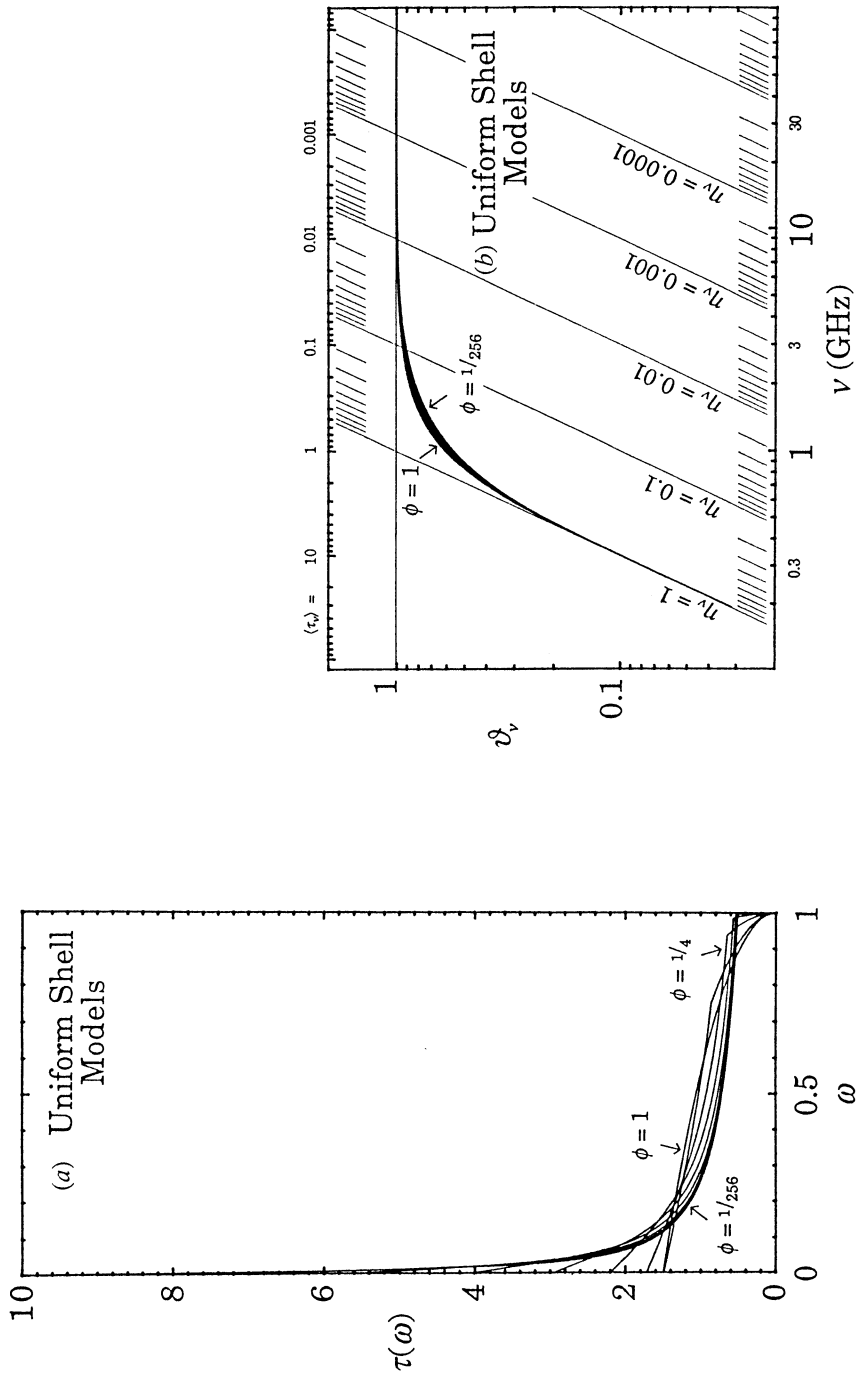

Fig. 5a. Profiles of $\tau(\omega)$ for shell models with $\phi = 1, 1/2, \ldots 1/256$. The case with $\phi = 1$ is a uniform sphere.
Fig. 5b. The spectra of ϑ_ν derived from the shell models of Fig. 5*a*.

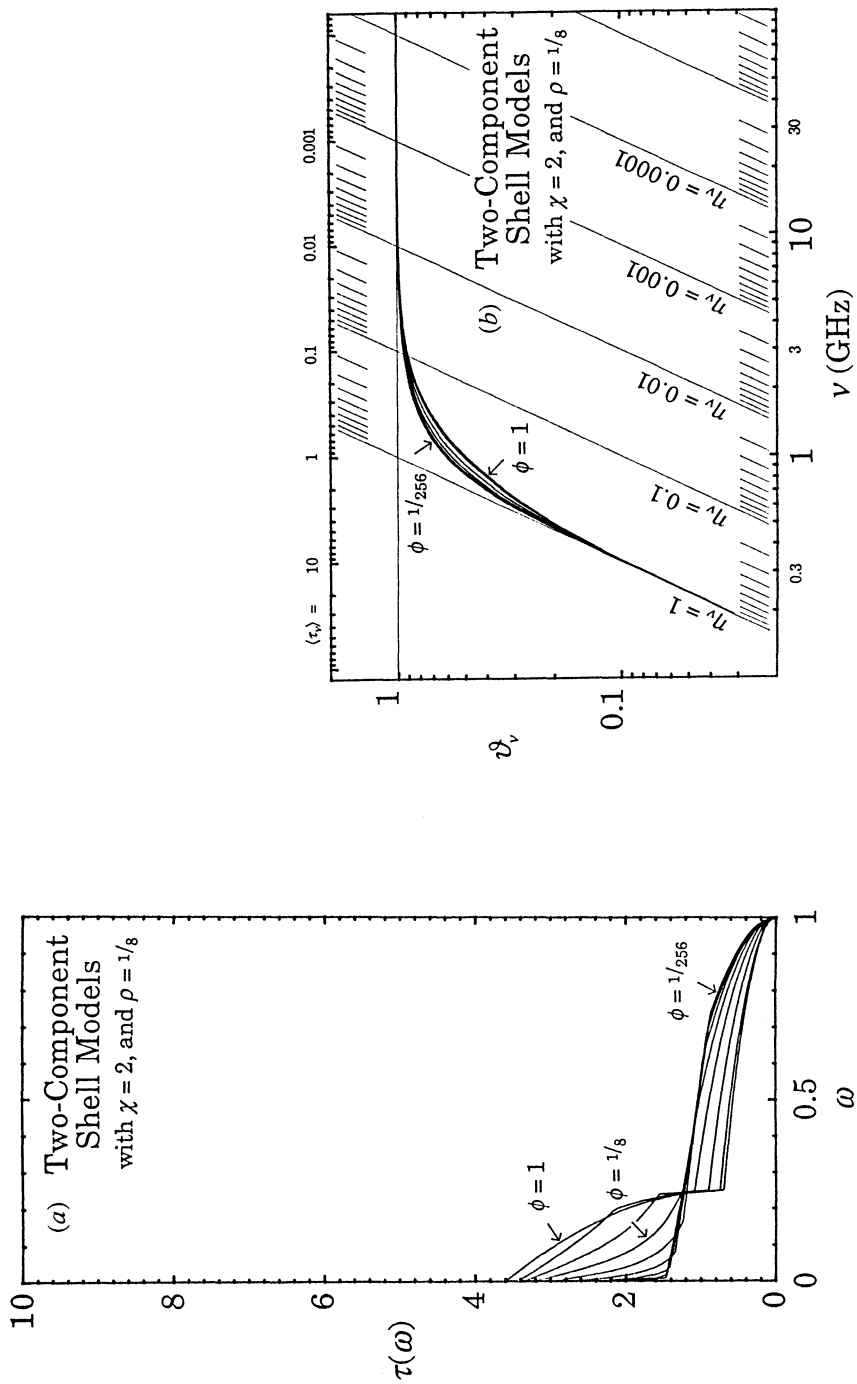

Fig. 6*a*. Profiles of $\tau(\omega)$ for two-component shell models with $\phi = 1, 1/2, \ldots 1/256$, $\chi = 2$, $\rho = 1/8$.
Fig. 6*b*. The spectra of ϑ_ν derived from the two-component shell models of Fig. 6*a*.

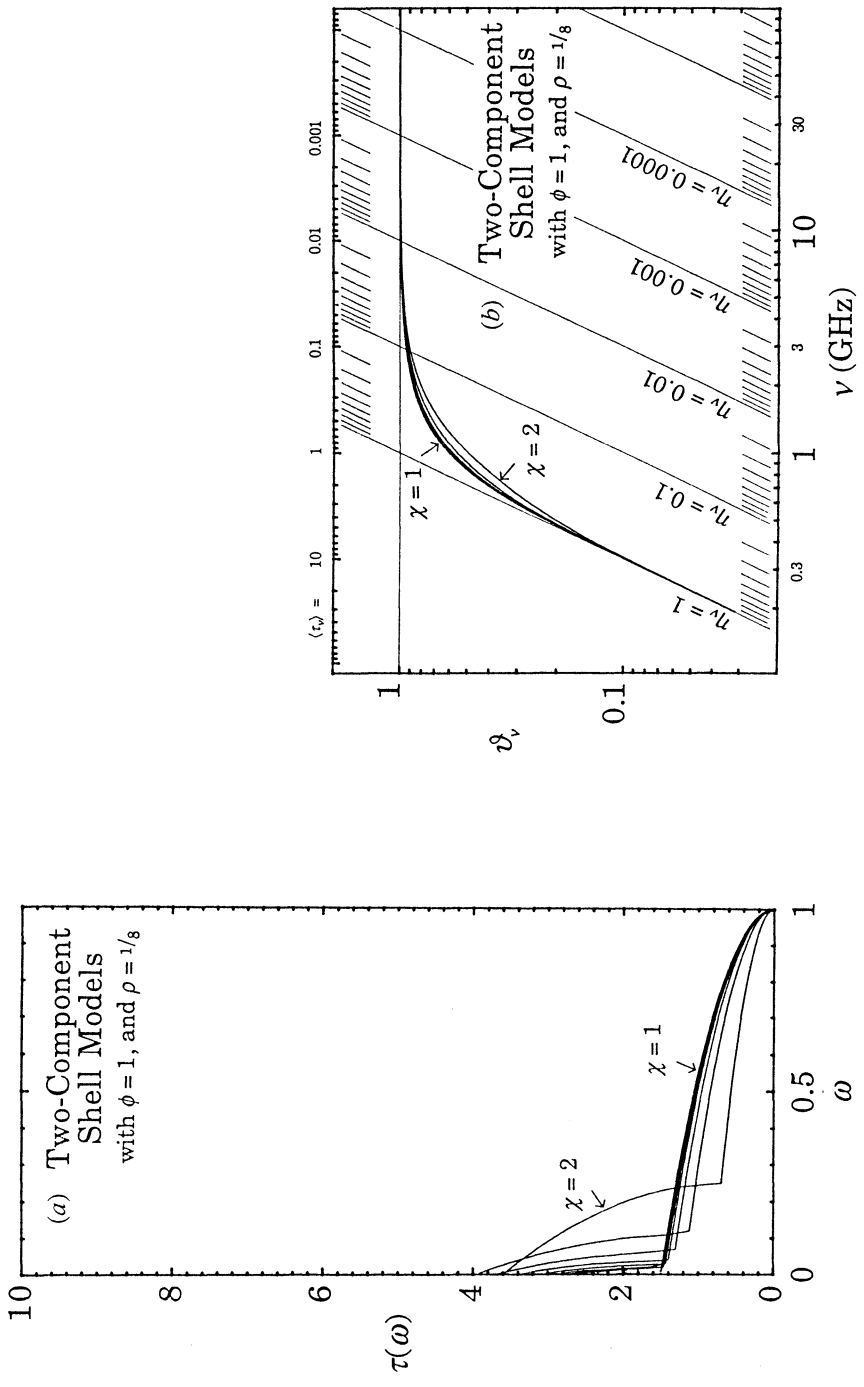

Fig. 7a. Profiles of $\tau(\omega)$ for two-component shell models with $\phi = 1$, $\chi = 1, 2 \ldots 10$, $\rho = 1/8$. The case $\chi = 1$ is virtually identical to $\chi = 10$.
Fig. 7b. The spectra of ϑ_ν derived from the two-component shell models of Fig. 7*a*.

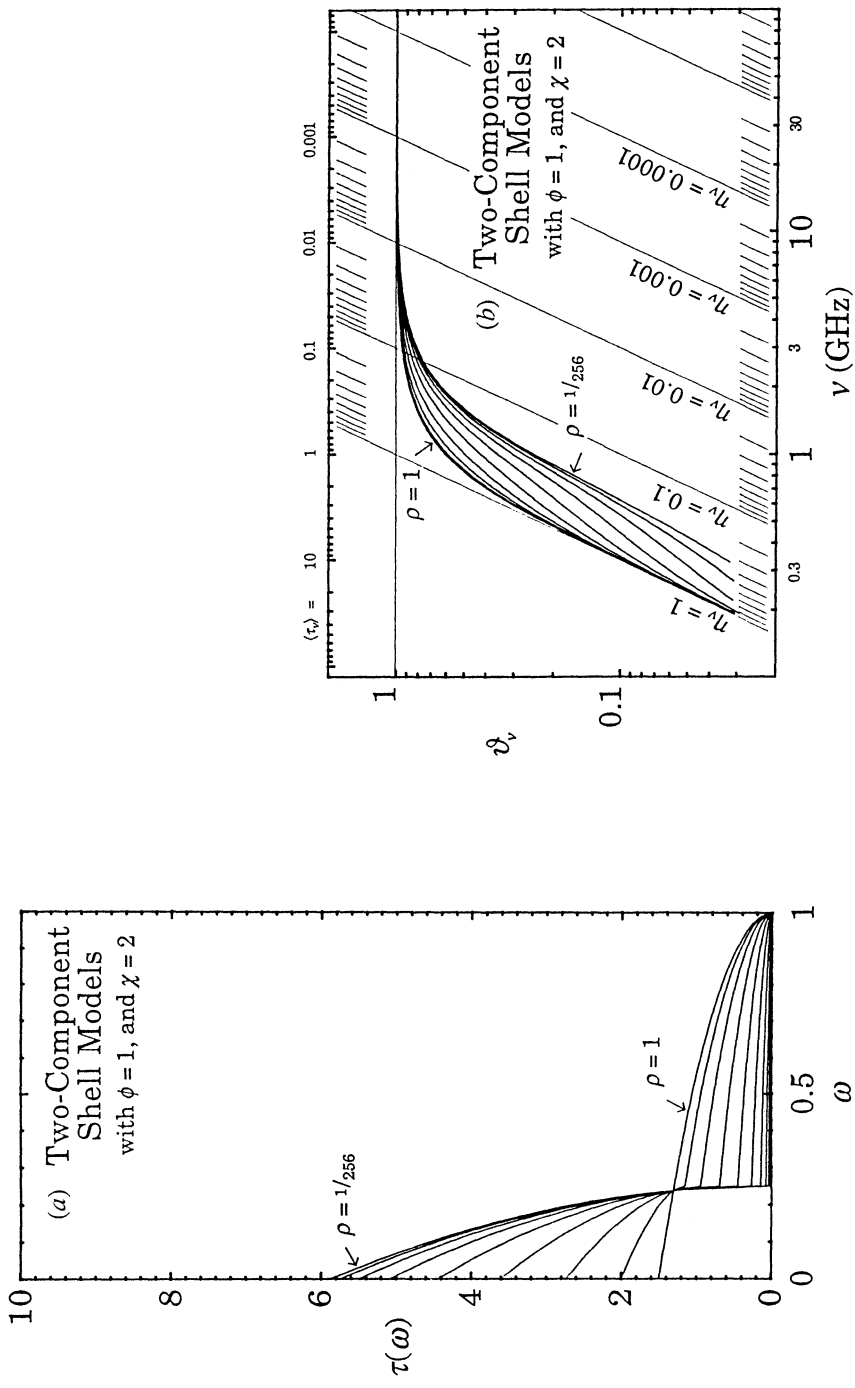

Fig. 8*a*. Profiles of $\tau(\omega)$ for two-component shell models with $\phi = 1$, $\chi = 2$, $\rho = 1, 1/2, \ldots 1/256$.
Fig. 8*b*. The spectra of ϑ_ν derived from the two-component shell models of Fig. 8*a*.

As shown by Fig. 5, there is very little difference between the radio spectra of the simple shell models. This arises from three effects. Firstly, the radio spectrum is insensitive to the three-dimensional distribution of the omitting material, since the optical depth arises from an integration along the line of sight. Secondly, we have the fact (mentioned above) that the actual two-dimensional distribution of optical depth is not important; all of the essential information can be expressed as a one-dimensional function $\tau(\omega)$. Thirdly, the radio spectrum is given as the Laplace transform of $\omega(\tau)$, and this tends to smear out detailed structures.

(f) Two-component Shell Models

This family of models combines elements of the core–halo models and the simple shells. The inner shell of thickness $0 \leq \phi \leq 1$ has unit radius and emissivity and is surrounded by a concentric shell of emissivity $0 \leq \rho \leq 1$ and outer radius $\chi \geq 1$.

Higgs (1971) used two-component shell models in his analysis of all radio flux densities available for planetary nebulae at that time. Approximate values of the three parameters were estimated from the nebular morphology of Hromov and Kohoutek (1968*a*, *b*, *c*). This is probably the limit of what can be done in matching model parameters to observed nebular structure. Beyond this it would be simpler to use nebular isophotes themselves.

With three parameters to vary it is obviously difficult to investigate this family of models fully. Assuming base values of $\phi = 1$, $\chi = 2$, and $\rho = 1/8$, Figs 6, 7 and 8 show what happens to the radio spectra as one parameter is varied while keeping the other two fixed.

4. Results for IC 418

Perhaps the best way to compare different models is to use them to fit the observed flux densities for a particular nebula and compare the results. The young planetary nebula IC 418 is one of the most frequently observed objects of its type, and has a well-defined radio continuum spectrum. It thus seems appropriate for use as a benchmark.

The flux densities for IC 418 were obtained from the following sources: all flux densities obtained from observations before 1971 from the compilation of Higgs (1971), thereafter Terzian *et al.* (1974), Gopal Sistla *et al.* (1974), Milne and Webster (1979), Milne (1979), Milne and Aller (1982), and Calabretta (1982). An unpublished measurement by the author of $0 \cdot 57 \pm 0 \cdot 06$ Jy at 843 MHz from the Molonglo Observatory Synthesis Telescope (MOST) was also used.

A wide range of models from the six families described above were applied to IC 418 using the procedure described in Section 2 with maximum likelihood estimation. The results are presented in Table 1, together with those obtained for the distribution of $\tau(\omega)$ derived from the Hβ isophotes of Reay and Worswick (1979). Fig. 9 shows the best fit spectra derived for the isophotes. IC 418 has been observed many times at frequencies near $0 \cdot 408$, $1 \cdot 420$, $2 \cdot 700$ and $5 \cdot 000$ GHz, and the data points in Fig. 9 have been shifted a little in the horizontal direction to avoid overlap. This is indicated in the figure by a brace which groups the data points together at the frequency corresponding to its cusp. The reference frequency for s_0 was taken at 1 GHz, the error

Table 1. Results of modelling IC418

Model	Parameters	ν_c (GHz)	s_0 (Jy)	$\mathcal{L}$	ν_t (GHz)
Uniform slab	None	1·49	1·87	−23·5	0·85
Core–halo	$\omega_c = 1/2$ $\rho = 1/2$	1·47	1·88	−22·6	0·85
	$\omega_c = 1/2$ $\rho = 1/4$	1·43	1·91	−21·7	0·89
	$\omega_c = 1/2$ $\rho = 1/8$	1·35	1·93	−22·6	0·90
	$\omega_c = 1/2$ $\rho = 1/16$	1·26	1·91	−23·3	0·91
	$\omega_c = 1/2$ $\rho = 1/32$	1·18	1·90	−22·7	0·90
	$\omega_c = 1/4$ $\rho = 1/8$	1·36	1·99	−24·6	0·92
	$\omega_c = 1/8$ $\rho = 1/8$	1·42	2·02	−23·8	0·89
Exponential	$\omega_e = 1/4$	1·33	1·96	−23·1	0·92
	$\omega_e = 1/8$	1·01	1·98	−25·8	0·94
	$\omega_e = 1/16$	0·73	1·98	−25·9	0·94
	$\omega_e = 1/32$	0·53	1·98	−25·9	0·95
Power law	$\delta = 0·01$ $\gamma = 3·5$	0·87	2·04	−36·9	1·01
	$\delta = 0·01$ $\gamma = 2·5$	0·74	2·09	−48·5	1·07
	$\delta = 0·01$ $\gamma = 1·5$	0·37	2·39	−135·4	1·48
Uniform shell	$\phi = 1$	1·46	1·88	−22·6	0·86
	$\phi = 1/2$	1·47	1·88	−22·7	0·86
	$\phi = 1/4$	1·47	1·88	−22·6	0·86
	$\phi = 1/8$	1·47	1·89	−22·3	0·86
	$\phi = 1/16$	1·46	1·91	−21·9	0·87
	$\phi = 1/256$	1·46	1·95	−21·5	0·87
Two-component shell	$\phi = 1$ $\chi = 2$ $\rho = 1/8$	1·39	1·97	−22·6	0·90
	$\phi = 1/2$ $\chi = 2$ $\rho = 1/8$	1·40	1·95	−21·5	0·90
	$\phi = 1/2$ $\chi = 2$ $\rho = 1/8$	1·46	1·89	−22·2	0·87
	$\phi = 1$ $\chi = 4$ $\rho = 1/8$	1·46	1·91	−21·9	0·87
	$\phi = 1$ $\chi = 8$ $\rho = 1/8$	1·46	1·89	−22·5	0·86
	$\phi = 1$ $\chi = 2$ $\rho = 1/2$	1·45	1·90	−22·1	0·87
	$\phi = 1$ $\chi = 2$ $\rho = 1/16$	1·30	2·01	−27·7	0·97
	$\phi = 1$ $\chi = 2$ $\rho = 1/32$	1·14	2·00	−33·8	1·00
Isophotes	None	1·19	1·95	−25·2	0·94

in ν_c is ±0·05 GHz, and in s_0 it is ±0·04 Jy. These errors correspond to the points where $\mathcal{L}$, the $\log_e$-likelihood, fell 0·5 below the maximum value, and are virtually model-independent. Also listed in Table 1 is the *turnover* frequency ν_t, defined as the frequency for which $\vartheta_\nu = 0·3$. This definition is intended to reflect a measurable property of the observed radio spectrum in the expectation that it will be largely model-independent.

5. Discussion

Values of the $\log_e$-likelihood listed in Table 1 should give some indication of the appropriateness of each model for IC418. The formal 3σ range should correspond to values of $\mathcal{L}$ between the maximum of −21·5, and −23·0. Clearly, the power-law models do not serve at all well, and the exponentials provide a poor fit for some values of ω_e. However, the small differences between the other models are proabably not significant, although it is interesting to note that $\tau(\omega)$ derived from the Hβ isophotes provides a poorer fit than some simpler models. The turnover in the observed spectrum seems to be somewhat steeper than that derived from the isophotes (which is somewhat

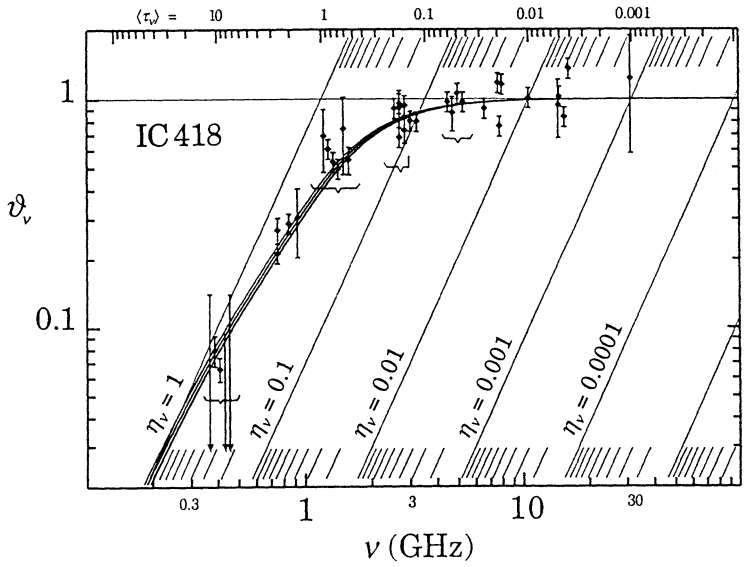

Fig. 9. Best fit model spectra of IC418 derived using the Hβ isophotes of Reay and Worswick (1979).

like an exponential), although not as steep as a uniform slab. The differences in the values of the $\log_e$-likelihood would be weighted heavily by a small number of flux densities in the turnover region of the spectrum, since this is principally where the model spectra differ.

Table 1 shows that, except for the power-law models, the best fit value of s_0 is little affected by the choice of model, ranging as it does from 1·87 to 2·02 Jy, or 1·95 Jy ±4%. This is quite understandable, since the optically thin part of the spectrum is well defined by the flux densities, and most models look the same in this regime.

However, the range of ν_c is rather wider. From a maximum of 1·49 GHz for the uniform slab it drops to 0·53 GHz for the exponential model with $\omega_e = 1/32$, and clearly it could be made arbitrarily smaller. The determining factor in the value of ν_c is the proportion of the model with very low values of τ. Thus for the exponential models, as ω_e decreases so does ν_c. Likewise, with the core–halo models and two-component shell models, as ρ decreases so does ν_c.

Excluding those models for which $\mathcal{L} < -30$, ν_t lies in the range 0·85 to 0·97 GHz, or 0·91 GHz ±7%. Considering the wide variation seen in the derived values of ν_c, that of ν_t is quite small. It is therefore a better indicator of the point where the spectrum starts to become optically thick.

Figs 1 to 8 show spectra derived from a wide range of quite different models. However, the one feature which distinguishes most clearly between them is the amount of low-level emission in $\tau(\omega)$. This can be seen in the core–halo models. Consider Figs 1*a* and 1*b*, which illustrate the core–halo models for $\omega_c = 1/2$ and $\rho = 1,\ 1/2,\ldots\ 1/512$. The case with $\rho = 1$ is a uniform slab, the model having the sharpest possible turnover. At the other extreme, the spectrum for $\rho = 1/512$ is virtually constrained to the locus of $\eta_\nu = 0{\cdot}5$, even

to quite low frequencies. Clearly only the core of this model is contributing any flux, the halo becoming visible only at much lower frequencies. It might be said to exhibit *pseudo-asymptotic* behaviour.

The core–halo model spectra in Figs 1*b* and 2*b* exhibit pseudo-asymptotic behaviour to some degree before making a transition to the true asymptote at $\eta_\nu = 1$. The spectrum with $\omega_c = 0 \cdot 1$ and $\rho = 1/64$ makes the transition in quite a pronounced way in Fig. 2*b*, and similar behaviour can be seen for the two-component shell models in Fig. 8*b*. The exponential models in Fig. 3*b*, however, do not make the transition from their pseudo-asymptotes within the range of frequency considered.

The rate at which the various model spectra approach their true asymptotes accounts for the wide range in the value of ν_c derived for IC 418. However, it was shown above that the turnover frequency ν_t is largely model-independent. The difference between these two frequencies is indicative of the relative amount of low-level emission in the models. Noting that ν_c/ν_t is constant for a given model, we can define a measure of the degree of clumping, C, associated with $\tau(\omega)$ as $C = \omega_c$, where the value of ω_c is that for which a core–halo model with $\rho = 0$ has the same values of ν_c and ν_t. It can be shown that

$$C = \left(0 \cdot 575 \frac{\nu_c}{\nu_t}\right)^{2 \cdot 1}, \tag{14}$$

where the value $0 \cdot 575$ is simply the ratio ν_t/ν_c for a uniform slab. This definition of the clumping factor may be compared with that of Terzian (1978).

Consider the temperature derived for IC 418 using the results of Table 1. Using equations (10) and (11) with $\Omega_s = 543$ arcsec^2 from the Hβ isophotes, we find T_e as low as 2060 K for a uniform slab, 3450 K for the isophotes, and as high as 19,200 K for the exponential model with $\omega_e = 1/32$. The different temperatures arise only from the different values of ν_c derived for each model.

Working backwards from the electron temperature of 9000±500 K derived from the forbidden optical emission lines by Barker (1979), we find that for $\Omega_s = 543$ arcsec^2 and $s_0 = 1 \cdot 95 \pm 0 \cdot 07$ Jy, we obtain $\nu_c = 0 \cdot 75 \pm 0 \cdot 03$ GHz. Combining this with the average turnover frequency $\nu_t = 0 \cdot 91 \pm 0 \cdot 06$ GHz, the measured clumping C_m is $0 \cdot 21 \pm 0 \cdot 05$. This value, which is largely model-independent, may be compared with the value $C_i = 0 \cdot 52$ obtained from $\nu_c = 1 \cdot 19$ GHz and $\nu_t = 0 \cdot 94$ GHz derived from the isophotes.

Seeing effects can broaden the measured value of Ω_s, so how much of the difference between C_m and C_i does this account for? The FWHM seeing for the isophotes of IC 418 used here was 2 arcsec. A fairly severe correction would be to reduce the effective radius of the nebula by 2 arcsec, thereby giving $\Omega_s = 390$ arcsec^2. Recomputation gives $\nu_c = 0 \cdot 88 \pm 0 \cdot 04$ GHz and a corrected value $C'_m = 0 \cdot 29 \pm 0 \cdot 07$, still disparate with respect to C_i.

The difference between C'_m and C_i is indicative of a degree of fine structure in the morphology of IC 418 which is not evident in the Hβ isophotes. As a measure of this unresolved structure we define

$$U = 1 - \frac{C'_m}{C_i}. \tag{15}$$

Thus if $U = 0$, all structure in the nebula has been resolved, while for $U = 1$, the opposite is true. For IC 418, $U = 0 \cdot 42$, which indicates that the present isophotes have failed to reveal quite a deal of the nebular structure.

Acknowledgments

I thank Professor B. Y. Mills and Dr A. J. Turtle for their comments. This work was undertaken while the author was in receipt of a Commonwealth Postgraduate Research Award.

References

Altenhoff, W. von, Mezger, P. G., Wendker, H., and Westerhout, G. (1960). *Veröff. Sternw.*, Bonn, No. 59, 48.
Barker, T. (1979). *Astrophys. J.* **219**, 914.
Calabretta, M. R. (1982). *Mon. Not. R. Astron. Soc.* **199**, 141.
Gopal Sistla, Kojoian, G., and Chaisson, E. J. (1974). *Astrophys. J.* **192**, 165.
Higgs, L. A. (1971). Catalogue of Radio Observations of Planetary Nebulae and Related Optical Data, Publ. Astrophys. Branch, Nat. Res. Council of Canada, Vol. 1, No. 1.
Hromov, G. S., and Kohoutek, L. (1968*a*). *Bull. Astron. Inst. Czech.* **19**, 1.
Hromov, G. S., and Kohoutek, L. (1968*b*). *Bull. Astron. Inst. Czech.* **19**, 81.
Hromov, G. S., and Kohoutek, L. (1968*c*). *Bull. Astron. Inst. Czech.* **19**, 90.
Mezger, P. G., and Henderson, A. P. (1967). *Astrophys. J.* **147**, 471.
Milne, D. K. (1979). *Astron. Astrophys. Suppl.* **36**, 227.
Milne, D. K., and Aller, L. H. (1982). *Astron. Astrophys. Suppl.* **50**, 209.
Milne, D. K., and Webster, B. L. (1979). *Astron. Astrophys. Suppl.* **36**, 169.
Olnon, F. M. (1975). *Astron. Astrophys.* **39**, 217.
Oster, L. (1961). *Astrophys. J.* **134**, 1010.
Panagia, N., and Felli, M. (1975). *Astron. Astrophys.* **39**, 1.
Pottasch, S. R. (1984). 'Planetary Nebulae: A Study of Late Stages of Stellar Evolution' (Reidel: Dordrecht).
Reay, N. K., and Worswick, S. P. (1979). *Astron. Astrophys.* **72**, 31.
Salem, M., and Seaton, M. J. (1974). *Mon. Not. R. Astron. Soc.* **167**, 493.
Terzian, Y. (1978). *In* 'Planetary Nebulae', IAU Symp. No. 76 (Ed. Y. Terzian), p. 111 (Reidel: Dordrecht).
Terzian, Y., Balick, B., and Bignell, C. (1974). *Astrophys. J.* **188**, 257.
Wright, A. E., and Barlow, M. J. (1975). *Mon. Not. R. Astron. Soc.* **170**, 41.

Manuscript received 19 November 1990, accepted 18 April 1991